Cell Docking in Double Grooves in a Microfluidic Channel**

*Masoud Khabiry, Bong Geun Chung, Matthew J. Hancock, Harish Chandra Soundararajan, Yanan Du, Donald Cropek, Won Gu Lee, and Ali Khademhosseini**

Microstructures that generate shear-protected regions in microchannels can rapidly immobilize cells for cell-based biosensing and drug screening. Here, a two-step fabrication method is used to generate double microgrooves with various depth ratios to achieve controlled double-level cell patterning while still providing shear protection. Six microgroove geometries are fabricated with different groove widths and depth ratios. Two modes of cell docking are observed: cells docked upstream in sufficiently deep and narrow grooves, and downstream in shallow, wide grooves. Computational flow simulations link the groove geometry and bottom shear stress to the experimental cell docking patterns. Analysis of the experimental cell retention in the double grooves demonstrates its linear dependence on inlet flow speed, with slope inversely proportional to the sheltering provided by the groove geometry. Thus, double-grooved microstructures in microfluidic channels provide shear-protected regions for cell docking and immobilization and appear promising for cell-based biosensing and drug discovery.

Keywords:
- cell docking
- cell patterning
- double grooves
- microfluidics

[*] M. Khabiry, Dr. B. G. Chung, Dr. M. J. Hancock, H. C. Soundararajan, Y. Du, Dr. W. G. Lee, Prof. A. Khademhosseini
Center for Biomedical Engineering
Department of Medicine, Brigham and Women's Hospital
Harvard Medical School
Boston, MA 02115 8 (USA)
E-mail: alik@mit.edu

M. Khabiry, Dr. B. G. Chung, Dr. M. J. Hancock, H. C. Soundararajan, Dr. Y. Du, Dr. W. G. Lee, Prof. A. Khademhosseini
Harvard-MIT Division of Health Sciences and Technology
Massachusetts Institute of Technology
Cambridge, MA 02139 (USA)

Prof. D. Cropek
U.S. Army Corps of Engineers
Construction Engineering Research Laboratory
Champaign, IL 61822 (USA)

1. Introduction

Microfluidic devices hold great promise for high-throughput screening and biochemical synthesis.[1–4] They enable the controlled manipulation of small amounts of fluid, important when costly reagents are employed, and are suitable for cellular applications due to their small size and high-throughput capability.[1,3,5,6] Moreover, the cellular micro-environment within microfluidic devices may be controlled by regulating different factors such as the flow rate and shear stress.[7,8] Microdevices with shear-protective grooved substrates enable cell docking, immobilization, and cell exposure to soluble factors, features necessary for cell-based applications such as drug discovery[9,10] and microbioreactors.[11,12] Previous microfabrication-based techniques for cell immobilization within microchannels include photocrosslinkable hydrogel patterning,[13,14] cup-shaped cell isolation arrays,[15] and microgrooved structures.[9,16] A previous study on single-grooved substrates found that cell positions and microcirculations could be controlled by varying the flow rate and the groove aspect ratio.[16] However, to our knowledge, no

systematic study exists of the effects of fluid flow and groove geometry on cell alignment.

In this manuscript, we report a microfluidic device containing a double-grooved substrate that enables multilevel control of cell docking and alignment. This simple yet adaptable microfluidic cell docking device should prove useful for cell patterning and generating co-cultures inside micro-channels. By adjusting the flow direction and the double-groove geometry, cells may be aligned in different groove corners. Also, double-layer spin-coating processes enable deeper grooves with higher aspect ratios to be fabricated than single-step photolithography techniques.

The goal of this paper is to analyze cell patterning and docking in double microgrooves. In particular, we link the cell docking locations to the microgroove geometry and estimate the effects of flow speed and geometry on cell retention. Computational simulations provide estimates of five characteristic flow patterns that are accurate proxies for cell docking. Simulations also predict the shear stress sheltering afforded by the double microgrooves. Experimental observations of cell alignment, docking, and retention in the double microgrooves are presented and analyzed, and related to the groove geometry and flow speed. Comparisons are made with previously reported results on single-grooved substrates. To provide general design criteria, the flow patterns and concomitant cell docking are predicted for double microgrooves of arbitrary geometry. Therefore, we quantify not only the additional sheltering engendered by double grooves but also the bi-modal cell-docking patterns that result in the upper and lower grooves.

2. Results and Discussion

A two-step photolithography method was used to fabricate the microfluidic device and its double-microgrooved substrate (Figure 1 and Experimental Section). SEM images of the double grooves are shown in Figure 2. Six geometries were fabricated involving two groove widths and three groove depth ratios (Figure 2c and Table 1).
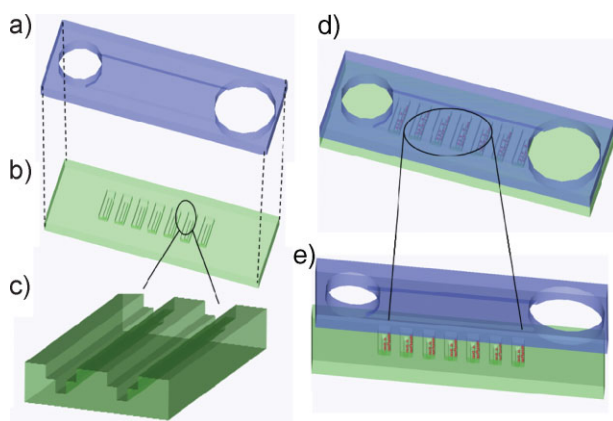

Figure 1. Schematic of the microfluidic device: a) Top channel configuration, b) bottom microgrooved surface, c) close-up of double grooves, d) microfabricated device with the cells docked in grooves, e) close-up of cells inside the grooves.
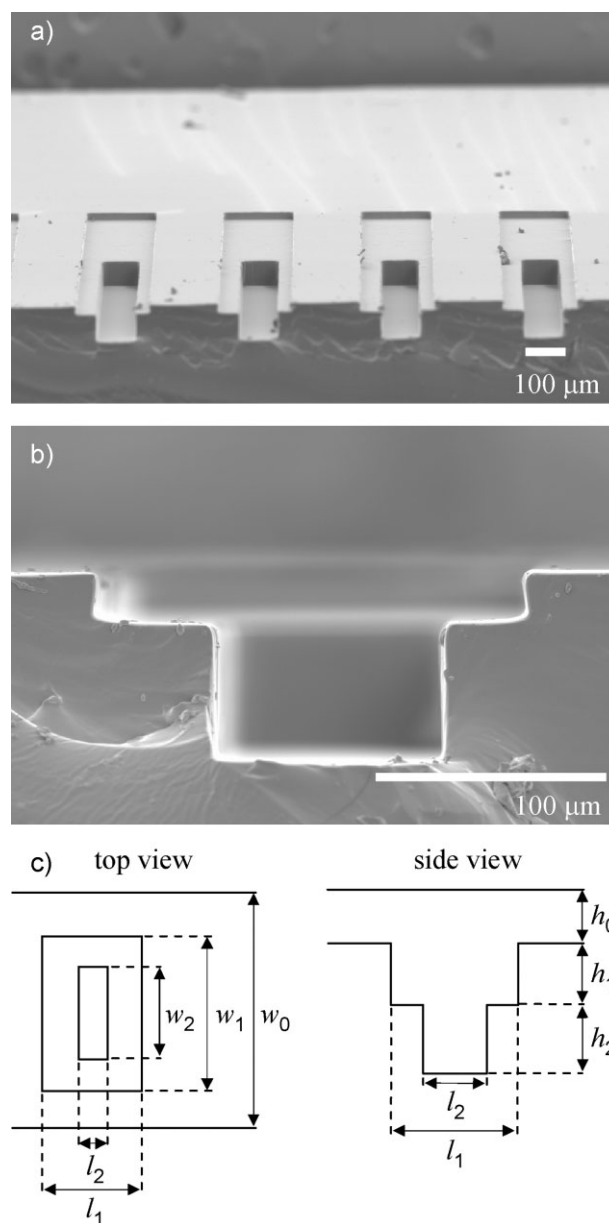

Figure 2. SEM images of a) double-grooved substrate and b) cross-section of double microgrooves. c) Schematic image of double-groove design, with inlet channel width w_0 and height h_0 and groove widths l_1, l_2, lateral lengths w_1, w_2, and heights h_1, h_2. Corresponding dimensions of fabricated double grooves listed in Table 1.

2.1. Theoretical Modeling

We employ a combined approach of dimensional analysis and numerical simulation to rationalize our experimental findings and to predict flow and cell docking patterns for double microgrooves of arbitrary geometry. Dimensional analysis is an efficient and systematic method of determining the dependence of flow patterns on the various geometrical and flow parameters. Computational fluid dynamics (CFD) is a powerful approach to solve many fluid dynamics problems.[17–20] Combined, these methods elucidate the dependence of the microcirculation pattern, shear stress, cell

Table 1. Dimensions of double grooves and inlet channels for fabricated grooved microfluidic device.

Geometry[a]	l_1 [μm]	l_2 [μm]	h_0 [μm]	h_1 [μm]	h_2 [μm]	w_0 [μm]	w_1 [μm]	w_2 [μm]
1	200	100	80	80	20	2000	1500	750
2				50	50			
3				20	80			
4	150	75	80	80	20			
5				50	50			
6				20	80			
M1,M2,M3,M4[b]	100, 75, 50, 25	0	40	40	0	4000	4000	0

[a] h_0, w_0 denote height, width of inlet channel, respectively; for grooves, l, h, w denote width, height, and lateral length and subscripts 1, 2 denote top and bottom grooves, respectively. Blank entries assume the value above.
[b] For comparison, channel with single grooves of Manbachi et al.[16]

Table 2. Dimensionless geometrical ratios for fabricated grooved microfluidic devices.

Geometry	h_0/l_1	h_2/h_1	$(h_{1+}h_2)/l_1$	l_2/l_1
1	0.40	0.25	0.5	0.5
2		1.0		
3		4.0		
4	0.53	0.25	0.67	0.5
5		1.0		
6		4.0		
M1[a]	0.40	0	0.40	0
M2[a]	0.53		0.53	
M3[a]	0.80		0.80	
M4[a]	1.60		1.60	

[a] Single-grooved channels of Manbachi et al.[16]

docking, and cell retention on the various geometric and flow parameters. Past research has characterized the flow patterns in single grooves[21–23] and guides the characterization of the analogous flow patterns in double grooves.

For the purpose of modeling, we assume the flow in the grooved microchannel is steady and two dimensional (2D). The flow is governed by the Navier–Stokes equations subject to appropriate boundary conditions (for details, see Section 4.). We scale all spatial variables by the width l_1 of the upper groove and scale flow velocities by the average inlet velocity $U = Q/(w_0 h_0)$. The flow in the double grooves is then specified by the five dimensionless ratios h_0/l_1, h_2/h_1, $(h_1 + h_2)/l_1$,

Table 3. Flow rates Q, inlet velocities U, and Reynolds numbers Re in fabricated grooved microfluidic devices.

Geometry	Q [μL min^{-1}]	U [cm s^{-1}]	Re
1–6	5	0.0521	0.0417
	10	0.1042	0.0833
	20	0.2083	0.1667
	30	0.3125	0.2500
	40	0.4167	0.3333
M1–M4[a]	5	0.0520	0.0208
	10	0.1040	0.0417
	20	0.2080	0.0833
	50	0.5210	0.2083
	75	0.7810	0.3125

[a] Single-grooved channels of Manbachi et al.[16]

l_1, and l_2/l_1 (Table 2) and the Reynolds number $Re = Q/(w_0 v)$ of the inlet channel (Table 3). In our experiments, the Reynolds number Re ranges from 0.04 to 0.33, and hence the flow is laminar and close to the Stokes flow limit, where the scaled velocities, shear stresses, and pressure gradients are purely dependent on geometry and not on the flow rate.[25]

2.1.1. Numerical Simulation of Flow Pattern in Double Grooves

The flow in the double grooves was simulated numerically (for details, see Section 4.) over a broad range of geometries (Figure 3a) and flow intensities, i.e., Reynolds numbers Re. In the parameter regime of interest, five characteristic flow patterns arise based on the type of microcirculation present in the bulk, and are presented in Figure 3b: i) corner eddies in the upper and lower grooves that are connected or ii) are connected separately on the upstream and downstream sides; iii) no circulation, iv) a double-eddy in bottom groove, and v) a single eddy in the bottom groove. Corner eddies exist in the four groove corners for all flow rates and geometries.[28] Simulations were run for a representative Reynolds number of $Re = 0.1$; virtually identical patterns exist for Re between 0 and 1. At these small Reynolds numbers, the streamline patterns and velocity contours all have approximate fore–aft symmetry, since the flow is close to the Stokes flow limit, which depends purely on the fore–aft symmetric double grooves. Cases (iii–iv) correspond to the fabricated geometries 4–6, respectively, listed in Tables 1 and 2, and differ only in groove depth ratio h_2/h_1. In general, narrow deep grooves contain eddies (Figure 3b(iv,v), $h_2/h_1 = 1,4$) while wide shallow grooves do not (Figure 3b(iii), $h_2/h_1 = 1/4$). The exception occurs for high inlet channels and wide grooves, i.e., large h_0/l_1, where corner eddies in the upper groove drive recirculation in the lower groove (Figure 3b(i), $h_0/l_1 = 0.53$, $h_2/h_1 = 0.1$). Reducing h_0/l_1 causes the recirculation to disappear (Figure 3b(ii), $h_0/l_1 = 0.50$, $h_2/h_1 = 0.1$). Lastly, Figure 3b(iii–v) also include the dimensionless velocity contour plots, which show that the magnitude of the velocity decreases rapidly into the sheltered microgrooves.

2.1.2. Bottom Shear Stress

Fluid shear stresses exerted on cells in microfluidic devices largely determine the docking pattern and retention. Cell adherence to channel surfaces decreases with increasing shear stress[29,30] and is also related to the flow behavior.[23,31–35] The
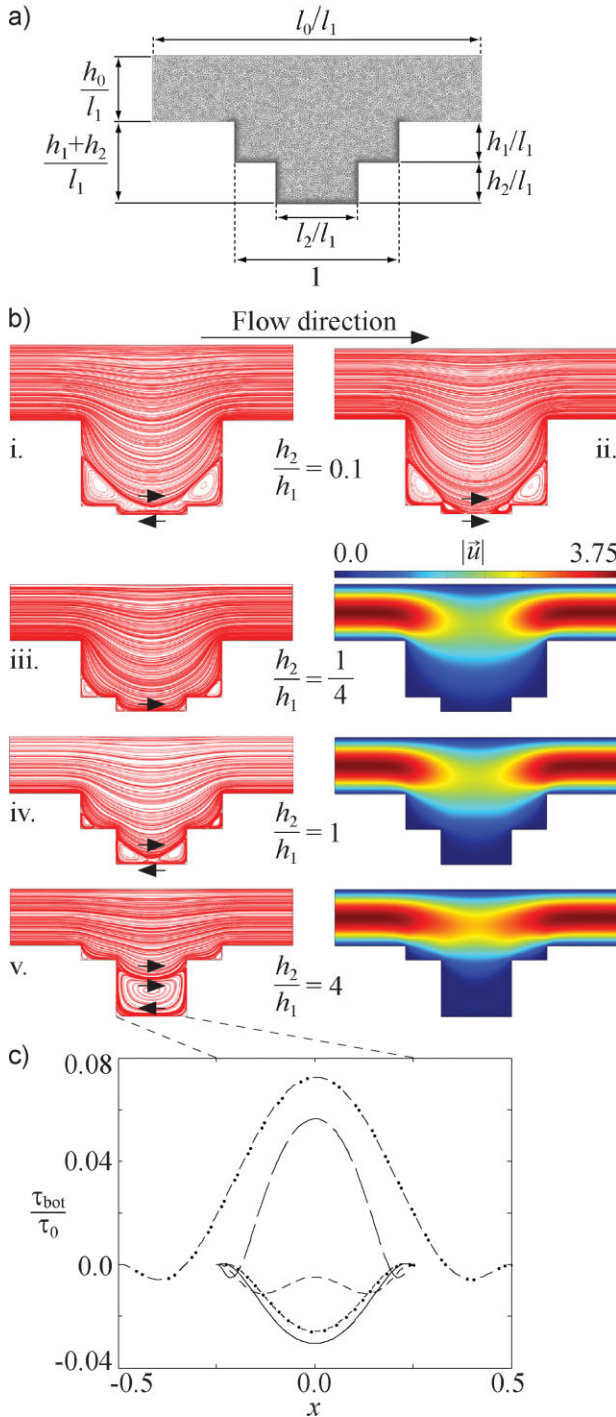
Figure 3. Numerical simulation of flow in double grooves. a) Computational domain including geometry and triangular mesh discretization. b) Streamlines and velocity contours for the five characteristic flow patterns in grooves with: depth ratios h_2/h_1 i–ii) 0.1, iii) 1/4, iv) 1, v) 4; scaled inlet heights h_0/l_1 i) 8/15, ii) 0.5, iii–v) 0.4, and scaled total depths $(h_1 + h_2)/l_1$ i–ii) 2/3, iii–v) 1/2. In all cases, $l_2/l_1 = 0.5$. Arrows indicate flow direction. c) Ratio of shear stress along the bottom groove, τ_{bot}, to that of the inlet channel, τ_0, for cases (iii–v), $h_2/h_1 = 1/4$ (——), 1 (– –), 4 (——). Corresponding profiles for single-groove limits $h_2/h_1 \to 0$ (– · · –) and $h_1/h_2 \to 0$ (– · –) are shown. x is the horizontal coordinate parallel to the flow and scaled with respect to the upper groove width.

cell docking patterns are given by the sign of the shear stress at the bottom boundaries of each groove. In Figure 3c we present the bottom shear stress in the lower groove, calculated via

$$\tau_{bot} = \rho v \frac{\partial u}{\partial y}\bigg|_{y=-h_1-h_2}. \tag{1}$$

We non-dimensionalize by the shear stress on the inlet channel wall given by the standard result for Poiseuille flow

$$\tau_0 = \frac{6\rho vQ}{w_0 h_0^2}, \tag{2}$$

where h_0 and w_0 are the channel inlet height and width, respectively. The bottom shear stress τ_{bot} is between 1% and 5% of that in the inlet channel, τ_0, less than that for a single groove of the outer width, but generally greater than that for a single groove of the inner width (Figure 3c). Also, τ_{bot}/τ_0 is smaller for deeper and narrower grooves, i.e., larger h_2/h_1 and smaller l_2/l_1. This is rationalized by noting that the total viscous dissipation in the bottom groove scales as $2\rho v e_{ij}^2 w_2 h_2 l_2 \sim \rho v U^2 w_2 h_2/l_2$, where e_{ij} is the rate of strain tensor and U is the inlet flow speed.[25] Thus as h_2 increases or l_2 decreases, the viscous dissipation is increased in the bottom groove, the flow speed is reduced and the sheltering effect enhanced.

Manbachi et al.[16] calculated the bottom shear stress in single grooves and have shown that it decreases as the grooves narrow. They have also demonstrated the linear dependence of bottom shear stress on inlet velocity U, and hence Reynolds number Re, as expected since the flow is close to the Stokes regime.

2.2. Experimental Results

This study provides both theoretical rationale and experimental evidence for cell alignment in a double grooved microfluidic device. Here, we present our experimental observations of cell alignment and retention and show that these correlate with the simulated flow direction and bottom shear stress magnitude in our microfluidic device.

2.2.1. Cell Docking in the Double Microgrooves

Experimental observations of cell docking and alignment in the four corners of the double grooves are presented in Figure 4a–c. The corresponding cell counts are presented in Figure 4d–g, sorted with respect to the docking position/flow pattern type for each fabricated double-groove geometry. Results for the two groove widths, $l_1 = 150$ and $200\,\mu m$, are similar. Also, similar cell counts are observed on the upper and lower grooves since the upper grooves are (laterally) longer than the lower grooves. Provided the cell diameter is small relative to the groove dimensions, cell docking and positioning are predicted solely based on the flow direction near the groove boundaries. The larger depth ratios h_2/h_1 are associated with microcirculation in the bottom cavity, resulting in cells lining the upstream corners of the grooves. Smaller depth ratios h_2/h_1 correspond to little or no microcirculation and hence cells align in the downstream corners of the grooves. Furthermore, cells were more
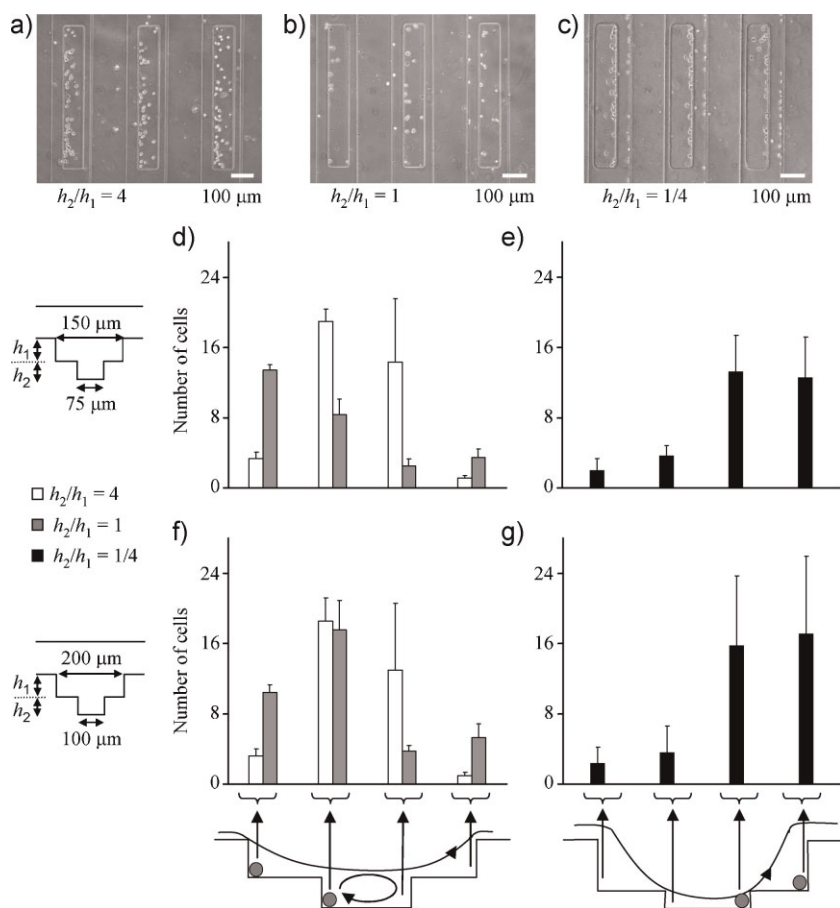
Figure 4. Cell docking in double microgrooves. a–c) Representative top views of cell positions on lower and upper microgroove surfaces for different geometries ($l_1 = 200\,\mu m$). d–g) Cell counts on upstream and downstream portions of upper and lower microgrooves, for geometries for narrower (d–e, $l_1 = 150\,\mu m$) and wider grooves (f–g, $l_1 = 200\,\mu m$). Schematics of experimental setup are shown left of charts, while those of the flow and cell docking patterns are shown below.

cell retention at a given inlet flow velocity U are desirable. Figure 5a–b presents the cell retention in the double microgrooves after exposure to a given inlet flow velocity U. Cell retention is observed to decrease approximately linearly with increasing inlet flow velocity. Moreover, cell retention is generally less on upper grooves than on lower grooves, since cells on the upper groove surface are more easily removed than those on the sheltered lower groove. Cell retention was higher for narrower and deeper grooves (larger $(h_1 + h_2)/l_1$ and h_2/h_1), which are associated with higher viscous dissipation and thus lower flow speeds and shear stresses, as discussed above.

The approximate linear dependence of cell retention on inlet velocity U and Reynolds number Re is rationalized by noting that cell mobility is proportional to shear stress[29] and, as discussed above, the shear stress at a particular location varies linearly with U (or Re). Hence, at a particular location, cell retention should vary linearly with U (or Re).

Cell retention also varies with location on the groove surface, with low retention associated with exposed outer edges and higher retention with sheltered corners. Thus, the effects of position and flow velocity U (or Re) are confounded in the cell-retention measurements derived from cell counts over entire grooves. These effects are partially separated in Figure 5c–d by plotting cell retention versus U, which seems to reveal one or two stages of cell removal. Consistent with our previous discussion, in each stage the retention has a linear dependence on U (or Re). Exposed cells are rapidly removed first (steep slope), followed by the slow removal of sheltered cells (mild slope). The cell retention on lower grooves (Figure 5c) is generally higher and more uniform, due to the relatively uniform sheltering, compared with that on upper grooves (Figure 5d). The trends noted for parts (a–b) are also evident in (c–d): retention is higher for narrow and deep grooves compared with wide and shallow grooves.

Lastly, the maximum cell retentions in the single groove designs of Manbachi et al.[16] are plotted in Figure 5c for comparison, and are generally lower than that in our double-grooved device for the same average flow speed U. Despite some of Manbachi et al.'s grooves having aspect ratios up to 1.6, their shallow groove depths of $40\,\mu m$ are of the same order as cell diameters. The cells were likely affected by the interior flows, rather than simply the small bottom shear stresses, thereby reducing retention. The ratio of cell diameter to groove depth should not be overlooked in microgroove design when cell retention is deemed important.
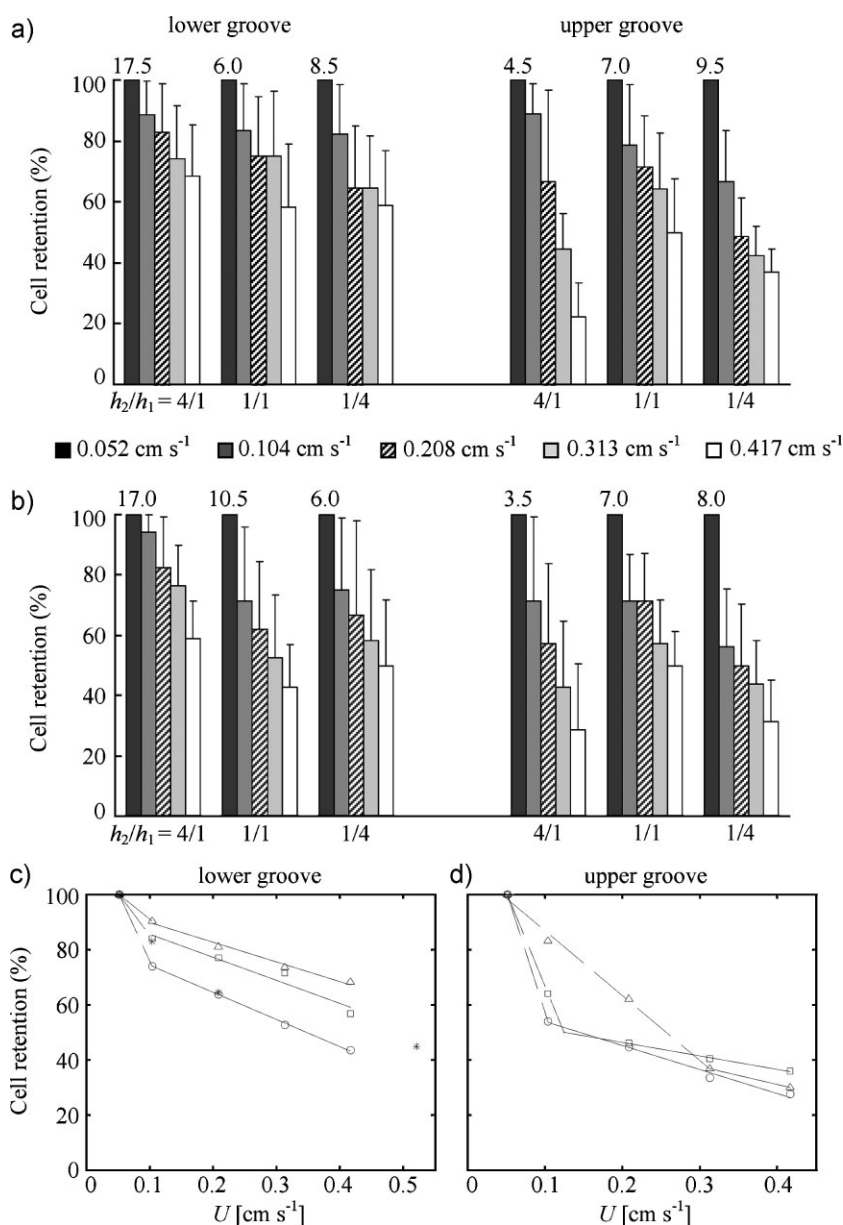
dispersed in the deeper bottom grooves as a result of the higher sheltering and weaker flows. To summarize, for cases where the cells are small relative to the groove dimensions, the microcirculation pattern is sufficient for predicting cell alignment.

When groove dimensions become the same order as the cell diameters, cells are affected by both the interior flow in the bulk and the bottom shear stress. In particular, the sign of the shear stress at the groove boundary may not be sufficient for determining the cell docking pattern. For example, the shallow lower grooves in geometry 4 (Table 1) are $20\,\mu m$ deep, the same order as the cell diameter. It is therefore not surprising that even though microcirculation is predicted to exist in the thin lower groove (Supporting Information Figure S1a), cells dock in the downstream corner of the lower groove as if unaffected by the reversed flow.

2.2.2. Cell Retention in the Double Microgrooves

Fluid flow through microfluidic devices delivers nutrients, growth factors, and reagents to the cells immobilized inside. However, exposing the cells to flow also leads to cell removal from the device. Therefore, groove designs that offer optimal

Figure 5. Experimental analysis of cell retention in double microgrooves. a–b) Cell retention for various inlet flow velocities U in a) narrow ($l_1 = 150\,\mu m$, $l_2 = 75\,\mu m$) and b) wide ($l_1 = 200\,\mu m$, $l_2 = 100\,\mu m$) microgrooves. Values are normalized by the number of cells in grooves at $U = 0.052\,cm\,s^{-1}$ listed over appropriate bar. c–d) Representative cell retention measurements as a function of U in c) lower grooves ($\triangle$ $l_2 = 75\,\mu m$, $h_2/h_1 = 4$; $\square$ $l_2 = 75\,\mu m$, $h_2/h_1 = 1$; $\bigcirc$ $l_2 = 100\,\mu m$, $h_2/h_1 = 1$) and d) upper grooves ($\triangle$ $l_1 = 200\,\mu m$, $h_2/h_1 = 4$; $\square$ $l_1 = 150\,\mu m$, $h_2/h_1 = 1/4$; $\bigcirc$ $l_1 = 200\,\mu m$, $h_2/h_1 = 1/4$). Fitted lines (– –, —) demonstrate the linear dependence on U for each stage of the cell-removal process. (*) indicates maximum retention for previously designed single groove devices.[16]

2.3. Classification of Flow Pattern and Cell Docking

We have shown experimentally that cell docking and alignment are determined by the microcirculation pattern. It is therefore important to relate the microcirculation pattern to the double-groove geometry and inlet flow speed U (or Reynolds number Re). To this end, we have constructed phase diagrams in Figure 6 of the microcirculation patterns in terms of the critical depth ratio h_2/h_1 and scaled inlet height h_0/l_1,

for various scaled total depths $(h_2 + h_1)/l_1$, groove width ratios l_2/l_1, and Reynolds numbers Re. The phase boundaries are found by binary search based on the signs of the shear stress at the fore–aft edges between the upper and lower grooves and at the middle of the lower groove. The binary search is stopped when the difference in parameter values separating two flow patterns is less than 0.001. The phase boundaries for the three Reynolds numbers $Re = 0$, 0.1, 1 plotted in Figure 6a–c virtually coincide, demonstrating the insensitivity to U (and Re). This is not surprising, as discussed above, since our parameter regime is close to Stokes flow, where the dimensionless flow pattern is dependent only on the groove geometry, not the inlet velocity. Figures 6a–b shows the phase diagrams corresponding to our fabricated double grooved channel geometries 1–3 and 4–6, respectively. The phase boundaries accurately separate the different cell-docking patterns, except for the leftmost data square in Figure 6a in which the cell diameter is comparable to the groove depth, as discussed above. Higher inlet aspect ratios h_0/l_1 and groove depth ratios h_2/h_1 are associated with recirculation, which is consistent with the behavior noted for single grooves since increasing h_2/h_1 effectively increases the aspect ratio h_2/l_2 of the lower groove. The phase boundary separating recirculation from no circulation approaches the corresponding single groove limit as $h_2/h_1 \rightarrow 0$, denoted by (*). A second phase boundary separates coupled and de-coupled eddies between the upper and lower grooves (straight lines in Figures 6a, b). This phase boundary has no analog in the single groove, and thus does not have a corresponding single-groove limit. The phase diagram for single grooves shows that higher inlet aspect ratios h_0/l_1 and groove aspect ratios h_1/l_1 are associated with recirculation (Figure 6c). The phase boundary accurately separates the flow and cell docking patterns observed by Manbachi et al.[16] The dependence of the phase boundaries on the double groove width ratio l_2/l_1 and scaled total depth $(h_2 + h_1)/l_1$ is shown in Figures 6d and e, respectively. Increasing the width ratio l_2/l_1 widens the lower groove, requiring a larger depth ratio h_2/h_1 for recirculation, thereby moving the phase boundary to the right in Figure 6d. Increasing the scaled total depth $(h_2 + h_1)/l_1$ increases the overall groove aspect ratio, reducing the depth ratio h_2/h_1 required for recirculation, thereby moving the phase boundary to the left in Figure 6e.
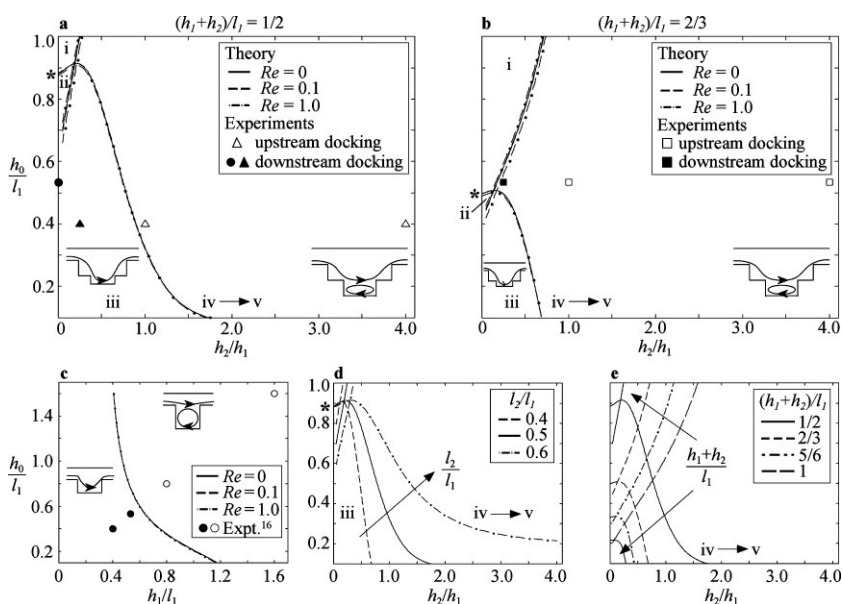
Figure 6. Phase diagrams of the characteristic flow patterns in the double groove with experimental results of docking patterns in double- and single- [16] groove geometries (parameters listed in Table 2). a) $(h_1 + h_2)/l_1 = 1/2$ with data for △ upstream, ▲ downstream docking, and ● single grooves [16] with downstream docking. (b) $(h_1 + h_2)/l_1 = 2/3$ with data for □ upstream and ■ downstream docking. c) Phase diagram for single grooves ($h_2 = 0$) with data[16] for ○ upstream and ● downstream docking. Flow patterns illustrated by schematics (insets) and denoted by roman numerals i–v corresponding Figure 3b. (*) denotes single-groove limit ($h_2 = 0$) of phase boundary. Dependence of phase boundaries on d) groove width ratio $l_2/l_1 = 0.4$ (– –), 0.5 (——), 0.6 (– · –) and e) total groove depth $(h_1 + h_2)/l_1 = 1/2$ (——), 2/3 (– –), 5/6 (– · –), 1 (long dash). Reynolds number Re in (a–c) is 0 (——), 0.1 (– –), 1.0 (– · –) and in (d–e) $Re = 0$. Vertical and horizontal axes of plots a,b,d,e are identical.

Misalignment between the centers of the upper and lower microgrooves (Figure 2b) breaks the symmetry of the groove geometry and the near symmetry of the flow. In the limit as the lower groove is shifted completely to one side, an edge and corner disappear along with the associated eddies. We have used numerical simulation to precisely assess the effects of misalignment on the flow pattern (see Supporting Information). These simulations demonstrate that misalignments of up to 1/8 of the upper groove width do not alter the characteristic flow patterns for designs that are relatively wide or have deep lower grooves. For the groove designs fabricated in this study, misalignments affect at most geometry 4 (Table 2), which is narrow with a shallow lower groove. As discussed above, cell docking occurred downstream despite the recirculation present in the lower groove; a shift of the bottom groove may have been partially responsible.

2.4. Cell Docking in Other Geometries

When fluid flows past a sharp corner in a grooved substrate, cells may be effectively docked and aligned if the corner affords sufficient shelter. In theory, a myriad of geometries may be employed to create various cell docking patterns, such as multigrooved substrates of rectangular, triangular, trapezoidal, or other cross sections (see Reference [16] and references therein). Computational flow simulations analogous to those presented here could help predict the docking patterns and the degree of shelter. The particular choice of

groove geometry depends not only on the concomitant cell-docking pattern but may also depend on the fabrication viability, mass-transport properties, and the area afforded for cell adhesion. Such features are important for the design of biosensors in order to deliver nutrients and diagnostic chemicals to docked cells.

3. Conclusions

Through a combined theoretical and experimental approach, we have demonstrated and rationalized cellular alignment and retention within double-grooved substrates in a microfluidic device. We have accurately linked the streamline pattern and shear stress direction to cell docking. We have constructed phase diagrams of the microcirculation pattern as a function of the four dimensionless ratios that specify the double-groove geometry. Thus, given a particular double-groove design, the microcirculation pattern may be found from the phase diagrams, allowing accurate estimates of the cell docking and alignment. We have also quantified the degree of cell retention in the upper and lower grooves and its dependence on groove geometry and its linear dependence on inlet flow speed. The larger depth of our grooves with respect to cell diameter also increases cell retention compared with that previously reported for single grooves. Double-grooved substrates provide controlled cell alignment while affording shear protection and high cell retention, and are thus ideally suited for cell-based biosensors and high-throughput drug screening.

4. Experimental Section

Fabrication method: Silicon master molds were created for the top fluidic channel and for the bottom double-microgrooved substrate. The master mold for the 80-μm-high top fluidic channel was made using a negative photoresist (SU-8 2050, Microchem, MA). The double-microgrooved substrates with varying groove depths (Table 1) were fabricated using a two-step photolithography method. The first layer of the microgroove patterns (groove depths $h_1 = 20$, 50, and 80 μm) were fabricated using negative photoresists (SU-8 2015, SU-8 2050). For the 20-μm-deep pattern, SU-8 2015 was spin-coated at 2,000 rpm for 30 s, baked for 3 min at 95 °C, and exposed to UV (140 mJ cm^{-2}) for 1 min. The 50- and 80-μm-deep patterns were fabricated by spin-coating SU-8 2050 at 2,600 rpm and 1,700 rpm for 1 min, respectively. The second layer of the groove patterns was fabricated by spin coating SU-8 2050 photoresist on a silicon wafer patterned with the first groove patterns. The total depth of the first and second layers was

100 μm and the depth ratios were $h_2/h_1 = 1/4$, 1 and 4. Following photolithography, negative replicas of the top fluidic channel and the bottom microgroove channel were molded in poly(dimethylsiloxane) (PDMS) (Sylgard 184 Silicon elastomer, Dow Corning, MI). The PDMS prepolymer mixed with silicone elastomer and curing agent (10:1 ratio) was poured on the silicon masters and cured at 70 °C for 2 h. The PDMS molds were subsequently peeled off the silicon masters. Inlet and outlet ports for cell loading and medium perfusion were created in the top fluidic channel using sharp punchers. The top fluidic channel and bottom double microgrooved substrate were aligned and irreversibly bonded using oxygen plasma (5 min at 30W, Harrick Scientific, NY).

Cell docking and retention in double grooves: A cardiac muscle cell line (HL-1) derived from the AT-1 mouse atrial cardiomyocyte tumor was used to study cell docking in the double microgrooves in our microfluidic device. HL-1 cells were cultured with medium in a humidified incubator (37 °C, 5% CO$_2$). The cell culture medium consisted of 87% Claycomb Medium, 10% Fetal Bovine Serum (FBS), 1% L-Glutamine, 1% Norepinephrine, and 1% Penicillin/Streptomycin. Cells were trypsinized and dissociated with the culture medium and then seeded at a concentration of 4×10^6 cells mL^{-1} through the inlet port in the microfluidic device. After 10 minutes of cell seeding, culture medium was infused through the inlet port using a syringe pump at flow rates Q ranging from 5 to 40 μL min^{-1}. These flow rates generated average inlet velocities $U = Q/(w_0\ h_0)$ ranging from 0.052 to 0.417 cm s^{-1} (Table 3). For cell-docking experiments, a constant flow rate of $Q = 5$ μL min^{-1} was used. For the cell-retention experiments, cells were docked in the double microgrooves and then exposed to the various inlet velocities listed above. We tested and analyzed cell docking and retention for the six double-grooved substrate designs listed in Table 1. For the cell-docking and retention experiments, the flow speed was held constant until steady state conditions were reached, and then images of cells in the double microgrooves were obtained using an inverted microscope (Nikon TE 2000-U, USA). For cell-docking experiments, cells in the four groove corners were counted for each double microgroove geometry. The experiments were repeated three times for each flow condition. For cell-retention experiments, cells in each groove were counted; the experiments were repeated three times.

Dimensional analysis and assumptions: For the purpose of modeling, we assume the flow in the microchannel and grooves is steady and 2D. The former assumption holds since the flow rates in the experimental setup are steady. The latter assumption is valid since their channel width is roughly ten times its height and the groove lengths are roughly ten times their groove widths and heights. 2D flow in double-grooved microchannels is characterized by 9 physical input parameters: 6 specify the geometry, i.e., inlet channel width w_0 and height h_0, upper and lower groove widths l_1, l_2 and heights h_1, h_2 (Table 1 and Figure 2c), and 3 specify the fluid, i.e., the flow rate Q (cm^3 s^{-1}) and the density ρ and kinematic viscosity ν of the culture medium, taken to be that of water[24] at 20 °C, $\rho = 1.0$ g cm^{-3} and $\nu = 0.01$ cm^2 s^{-1}.

Dimensional analysis reduces the dependence of the 2D flow in double-grooved channels from 9 physical input parameters to 5 dimensionless parameters: 4 aspect ratios h_0/l_1, h_2/h_1, $(h_1 + h_2)/l_1$, and l_2/l_1 (Table 2) and the Reynolds number $Re = Q/(w_0\ \nu)$ of the inlet channel. For comparison, the flow in a single-grooved channel is completely described by 3 dimensionless parameters, h_0/l_1, h_1/l_1 and Re. In our experiments, the Reynolds number Re ranges from 0.04 to 0.33 (Table 3). At these small Reynolds numbers, the flow is laminar and close to the Stokes flow limit, where the scaled velocities, shear stresses, and pressure gradients are purely dependent on geometry and not on the flow rate.[25] Introducing and working in dimensionless co-ordinates not only reduces the apparent complexity of the problem by half but also elucidates the flow regime and simplifies the dependencies expected in the numerical simulations.

Governing equations: The Navier–Stokes equations, which consist of the incompressibility condition and the conservation of momentum, govern the fluid flow. Motivated by the previous section, we solve the problem in dimensionless variables. We scale all spatial variables by the width l_1 of the upper groove and we scale flow velocities by the inlet velocity $U = Q/(w_0\ h_0)$ and pressure by $\rho\nu U/l_1$. In dimensionless variables, the steady Navier–Stokes equations become[26]

$$\vec{\nabla} \cdot \vec{v} = 0, \tag{3}$$

$$Re\,\vec{v} \cdot \vec{\nabla}\vec{v} = -\vec{\nabla}p + \nabla^2\vec{v}, \tag{4}$$

where $\vec{v} = (u, v)$ is the 2D velocity vector, u, v are the horizontal (longitudinal, x-direction) and vertical (y-direction) velocity components, p is the modified pressure due to dynamic effects,[25] $\vec{\nabla}$ the gradient operator and ∇^2 the Laplacian operator. The no-slip boundary condition is applied at the top and bottom walls. We assume the velocity profile in the inlet channel is fully developed Poiseuille flow. For the low Reynolds numbers in the parameter regime of interest, the flow in the inlet channel becomes fully developed over a distance h_0 away from the ports and grooves.[27] We impose the Dirichlet boundary condition $u = u_0$, $v = 0$ at the inlet, where the scaled inlet velocity u_0 has the Poiseuille profile

$$u_0 = 6\left(\frac{l_1}{h_0}\right)^2 y\left(1 - \frac{l_1 y}{h_0}\right), \tag{5}$$

and y is the dimensionless vertical coordinate. The modified pressure is set to zero at the outflow boundary (Dirichlet boundary condition).

Numerical simulation and domain discretization: In the present work, the commercial finite element package Comsol 3.4 (Comsol Inc., Burlington, MA) was used to conduct our numerical simulations. The 2D computational domain is discretized into an unstructured mesh of triangular elements (Delaunay triangulation, Figure 3a). Since the flow is fully developed in the top channel, the particular choice of the top channel length l_0 is immaterial and does not affect the results. The scaled top channel length l_0/l_1 is set to between 2 and 4, large enough for numerical convergence. The maximum mesh edge length was set to 0.025 in the bulk and 0.0025 at all corners and groove edges. The default convergence criteria in Comsol's static FEM solver were employed. Though the number of elements varies with the geometrical parameters, approximately 15,000 to 25,000 mesh elements and 1000 boundary elements were used in a single computation.

[1] A. Khademhosseini, R. Langer, J. Borenstein, J. P. Vacanti, *Proc. Natl. Acad. Sci. USA*. **2006**, *103*, 2480–2487.

[2] K. R. King, C. C. J. Wang, M. R. Kaazempur-Mofrad, J. P. Vacanti, J. T. Borenstein, *Adv. Mater.* **2004**, *16*, 2007–2012.

[3] G. M. Whitesides, *Nature* **2006**, *442*, 368–373.

[4] D. B. Weibel, G. M. Whitesides, *Curr. Opin. Chem. Biol.* **2006**, *10*, 584–591.

[5] D. J. Beebe, G. A. Mensing, G. M. Walker, *Annu. Rev. Biomed. Eng.* **2002**, *4*, 261–286.

[6] J. Melin, S. R. Quake, *Annu. Rev. Biophys. Biomol. Struct.* **2007**, *36*, 213–231.

[7] S. Takayama, E. Ostuni, P. LeDuc, K. Naruse, D. E. Ingber, G. M. Whitesides, *Nature* **2001**, *411*, 1016.

[8] A. Tourovskaia, X. Figueroa-Masot, A. Folch, *Lab Chip* **2005**, *5*, 14–19.

[9] A. Khademhosseini, J. Yeh, G. Eng, J. Karp, H. Kaji, J. Borenstein, O. C. Farokhzad, R. Langer, *Lab Chip* **2005**, *5*, 1380–1386.

[10] A. Khademhosseini, J. Yeh, S. Jon, G. Eng, K. Y. Suh, J. A. Burdick, R. Langer, *Lab Chip* **2004**, *4*, 425–430.

[11] J. Park, F. Berthiaume, M. Toner, M. L. Yarmush, A. W. Tilles, *Biotechnol. Bioeng.* **2005**, *90*, 632–644.

[12] P. J. Lee, P. J. Hung, L. P. Lee, *Biotechnol. Bioeng.* **2007**, *97*, 1340–1346.

[13] W. G. Koh, L. J. Itle, M. V. Pishko, *Anal. Chem.* **2003**, *75*, 5783–5789.

[14] A. Khademhosseini, K. Y. Suh, S. Jon, G. Eng, J. Yeh, G. J. Chen, R. Langer, *Anal. Chem.* **2004**, *76*, 3675–3681.

[15] D. Di Carlo, N. Aghdam, L. P. Lee, *Anal. Chem.* **2006**, *78*, 4925–4930.

[16] A. Manbachi, S. Shrivastava, M. Cioffi, B. G. Chung, M. Moretti, U. Demirci, M. Yliperttula, A. Khademhosseini, *Lab Chip* **2008**, *8*, 747–754.

[17] S. V. Patankar, *Numerical heat transfer and fluid flow*, Hemisphere, New York **1980**.

[18] J. H. Ferziger, M. Peric, *Computational methods for fluid dynamics*, Springer, New York **2002**.

[19] T. J. Chung, *Computational Fluid Dynamics*, Cambridge University Press, **2002**.

[20] D. A. Boy, F. Gibou, S. Pennathur, *Lab Chip* **2008**, *8*, 1424–1431.

[21] P. N. Shankar, M. D. Deshpande, *Annu. Rev. Fluid Mech.* **2000**, *32*, 93–136.

[22] S. Taneda, *J. Phys. Soc. Japan* **1979**, *46*, 1935–1942.

[23] J. J. L. Higdon, *J. Fluid Mech.* **2006**, *159*, 195–226.

[24] H. Singh, E. S. Ang, T. T. Lim, D. W. Hutmacher, *Biotechnol. Bioeng.* **2007**, *97*, 1291–1299.

[25] G. K. Bachelor, *An introduction to fluid dynamics*, The University Press, Cambridge 1967, pp. 126, 153, 217.

[26] C. Pozrikidis, *Boundary Integral and Singularity Methods for Linearized Viscous Flow*, Cambridge University Press, 1992, pp. 1.

[27] F. M. White, *Viscous Fluid Flow*, Mcgraw–Hill, Boston **1991**, pp. 114 (Equation 3–28).

[28] D. J. Acheson, *Elementary Fluid Dynamics*, Oxford University Press, 1990, pp. 229.

[29] D. P. Gaver, 3rd, S. M. Kute, *Biophys. J.* **1998**, *75*, 721–733.

[30] H. Lu, L. Y. Koo, W. M. Wang, D. A. Lauffenburger, L. G. Griffith, K. F. Jensen, *Anal. Chem.* **2004**, *76*, 5257–5264.

[31] J. A. Prins, J. Mulder, J. Schenk, *Appl. Sci. Res.* **1951**, *2*, 431–438.

[32] J. R. Sellars, M. Tribus, J. S. Klein, *Trans. ASME* **1956**, *78*, 441–448.

[33] C. Pozrikidis, *J. Fluid Mech.* **2006**, *180*, 515–527.

[34] U. Ghia, K. N. Ghia, C. T. Shin, *J. Comput. Phys.* **1982**, *48*, 387–411.

[35] E. Erturk, T. C. Corke, C. Gokcol, *Int. J. Numer. Meth. Fl.* **2005**, *48*, 747–774.